ACSNANO

www.acsnano.org

ARTICLE

Introducing Semiconducting-to-Metallic Transitions into Wafer-Scale 2D $PdSe_2$ Layers by Low-Temperature Anion Exchange and Thickness Modulation

Alireza Ghanipour, Sang Sub Han, Changhyeon Yoo, Chung Won Lee, and Yeonwoong Jung*

Cite This: *ACS Nano* 2024, 18, 35336–35346

Read Online

ACCESS | Metrics & More | Article Recommendations | Supporting Information

ABSTRACT: Two-dimensional (2D) palladium diselenide ($PdSe_2$) layers are projected to exhibit a number of intriguing electrical properties such as semiconducting-to-metallic transitions. Precisely modulating their morphology and chemistry is essential for realizing such opportunities, which is particularly demanded on a large dimension under flexible processing conditions toward broadening their practical device applicability. Herein, we explore a wafer-scale growth of 2D $PdSe_2$ layers and introduce semiconducting-to-metallic transitions into them at as low as 330 °C, a temperature compatible with a range of polymeric substrates as well as the back-end-of-line (BEOL) processes. Two independent physical and chemical approaches of thickness modulation and anion exchange are demonstrated to induce the low-temperature-driven electrical transitions. Wafer-scale 2D $PdSe_2$ layers grown from a scalable selenization of thin (~2 nm) Pd exhibit *p*-type semiconducting characteristics, which completely vanish with increasing thickness. Furthermore, a postgrowth reaction involving an exchange of selenium (Se)-to-tellurium (Te) ions chemically introduces the semiconducting-to-metallic transitions through the conversion of $PdSe_2$-to-palladium ditelluride ($PdTe_2$). A significant reduction of the bandgap energy from 0.7 to 0 V is observed to be associated with the transitions, while the converted 2D layers remain to be highly metallic irrespective of thickness variations. These controlled transition characteristics are employed to fabricate "all-2D" flexible devices employing semiconducting 2D layer channels and metallic 2D layer electrodes on a wafer-scale.

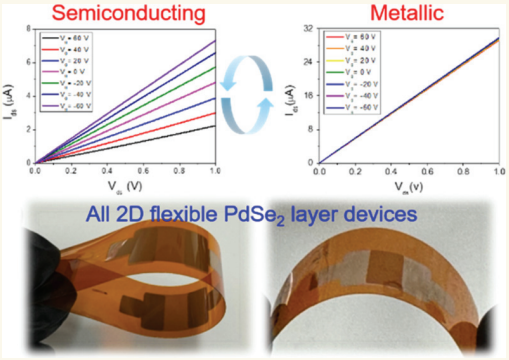

KEYWORDS: *2D TMD, $PdSe_2$, $PdTe_2$, anion exchange, thickness control, semiconducting-to-metallic transition*

INTRODUCTION

Investigations of two-dimensional (2D) transition metal dichalcogenide (TMD) layers have rapidly accelerated with emphasis on unveiling their morphology- and/or chemistry-dependent transitions of electrical and optical properties. A number of 2D TMD layers have been identified to exhibit such transition characteristics (e.g., layer number-dependent tunability of bandgap energy), mostly in those employing group VI transition metals such as molybdenum (Mo) and tungsten (W).[1,2] Recently, group X elements (e.g., platinum (Pt) and palladium (Pd)) have emerged as the transition metal components for 2D TMDs owing to their distinct advantages over the conventional VI metals. For example, their significantly lower melting temperatures enable the direct chemical reaction and growth of 2D layers even on polymeric substrates.[3−6] Furthermore, group X-based 2D TMD layers are also projected to exhibit the aforementioned layer morphology-dependent transient characteristics, mostly predicted by theoretical studies.[7,8] Among them, Pd-based TMDs such as 2D palladium diselenide ($PdSe_2$) layers exhibit favorable properties over Pt-based ones mainly due to the easier processability of Pd with low cost and ambient stability.[9] In fact, 2D $PdSe_2$ layers are particularly attractive for digital electronics with a large set of process-property advantages; for example, tunable bandgap energies accompanying semiconducting-to-metallic transitions[10−14] and low-temperature manufacturability.[15−20] Synthesis of 2D $PdSe_2$ layers with

Received: August 22, 2024
Revised: November 30, 2024
Accepted: December 10, 2024
Published: December 17, 2024

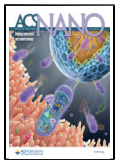

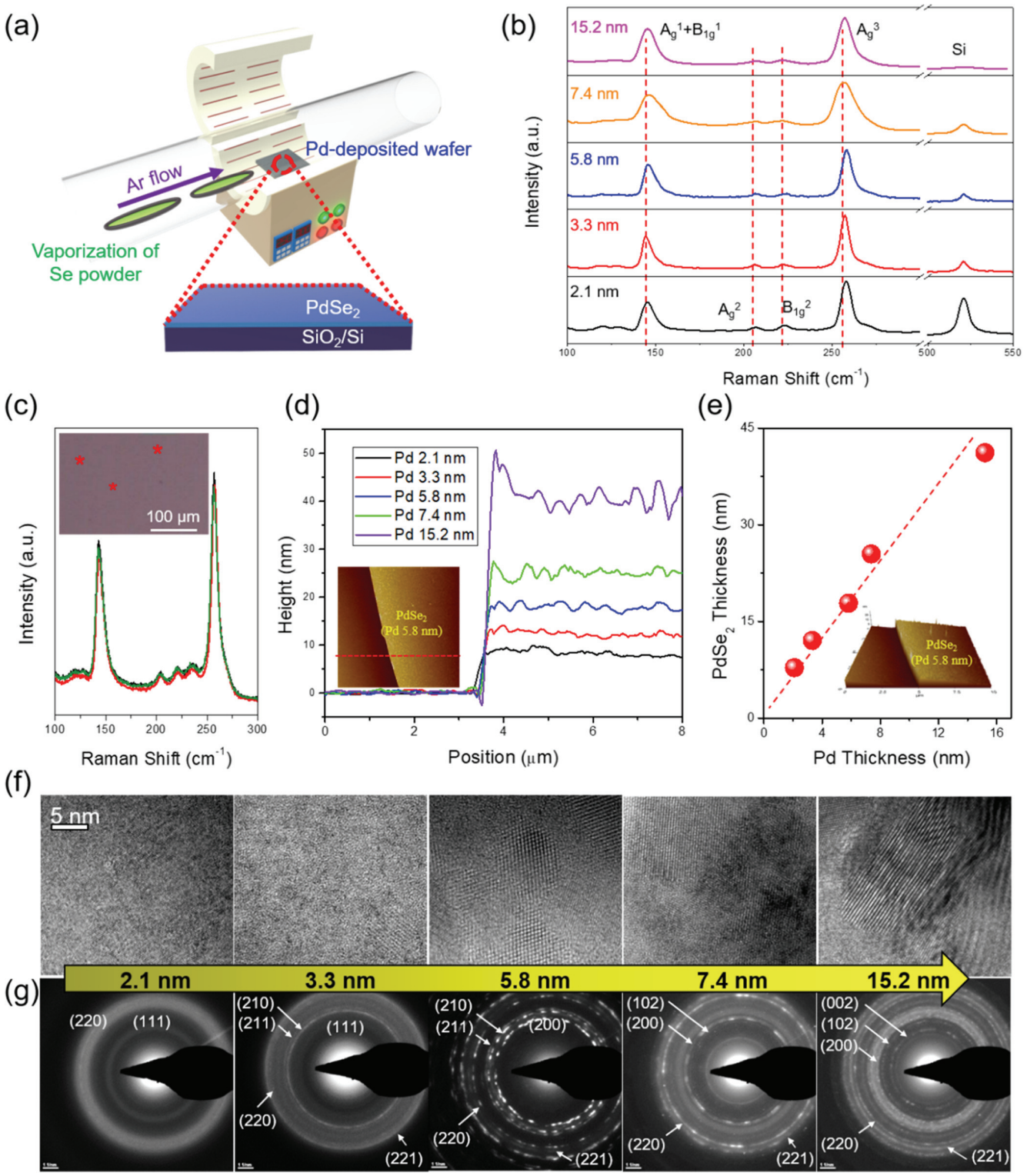

Figure 1. Thickness-variant growth and characterization of 2D $PdSe_2$ layers. (a) Schematic for CVD growth of 2D $PdSe_2$ layers. (b) Raman spectra of 2D $PdSe_2$ layers prepared with five different Pd thicknesses. (c) Raman spectra obtained from various locations of an identical sample prepared with Pd thickness of 2.1 nm. The inset shows an optical microscopy image of the sample. (d) AFM height profiles of 2D $PdSe_2$ layers prepared with five different Pd thicknesses along with a representative AFM topography image (inset). (e) Correlation of Pd thickness with resulting 2D $PdSe_2$ layers' thickness along with a representative AFM topography image (inset). (f), (g): TEM characterizations of thickness-variant 2D $PdSe_2$ layers manifested by (f) HR-TEM and (g) SAED images.

desired thickness and crystallinity has been explored with a variety of methods, among which, a chemical vapor deposition (CVD) is promising due its process scalability of guaranteeing a high spatial uniformity.[21−23] This intrinsic advantage can facilitate systematic studies on the structure−property relations of 2D $PdSe_2$ layers, vastly broadening their application aspects

https://doi.org/10.1021/acsnano.4c11627
ACS Nano 2024, 18, 35336−35346

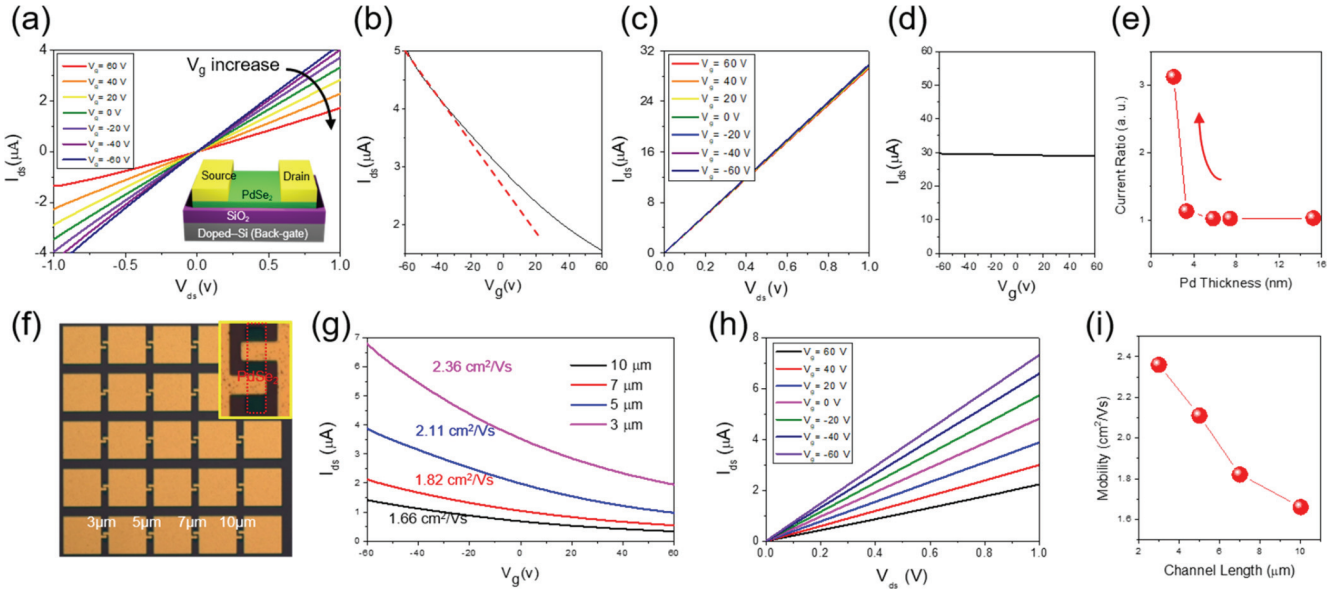

Figure 2. Semiconducting-to-metallic transition in thickness-variant 2D $PdSe_2$ layers manifested by FET measurements. (a) I_{ds}–V_{ds} curves with varying V_g obtained from a FET employing thin 2D $PdSe_2$ layers (Pd thickness = 2.1 nm). (b) I_{ds}–V_g curve obtained from the same FET in (a) at V_{ds} = 1 V along with its device schematic (inset). (c) I_{ds}–V_{ds} curves with varying V_g obtained from a FET employing thick 2D $PdSe_2$ layers (Pd thickness = 7.4 nm). (d) I_{ds}–V_g curve obtained from the same FET in (c) at V_{ds} = 1 V. (e) Comparison of I_{ds} ratios at V_g = ±60 as a function of Pd thickness. (f) Optical microscopy image of patterned FET array. (g) I_{ds}–V_g curves with varying channel lengths. (h) V_g-dependent I_{ds}–V_{ds} curves obtained from 3 μm channel FET. (i) Correlation of mobility value vs channel length.

in electronics, optoelectronics and beyond.[24−30] Modulating the morphology and chemistry of wafer-scale 2D $PdSe_2$ layers during and/or after their growth stages is essential toward tuning their resulting electrical and optical properties. This approach mainly aims at unveiling their coexisting semiconducting and metallic transport properties; i.e., semiconducting and metallic 2D layers function as active channels and passive electrodes for digital electronics, respectively.

Herein, we report a wafer-scale (>cm^2) CVD growth of 2D $PdSe_2$ layers via a direct selenization of Pd seed films at growth temperature as low as 330 °C. By leveraging their precisely controlled composition and morphology, we systematically introduce strong semiconducting-to-metallic transitions into them via two independent physical and chemical methods; i.e., thickness modulation and anion exchange of Se-to-Te, respectively. Regarding the physical method, thinner 2D $PdSe_2$ layers prepared with Pd films of <3 nm thickness display notable semiconducting characteristics accompanying a hole mobility of 2.32 $cm^2/V{\cdot}s$ while thicker ones remain metallic irrespective of thickness variations. Regarding the chemical method, the thin semiconducting 2D $PdSe_2$ layers are demonstrated to be converted to metallic stoichiometric 2D palladium ditelluride ($PdTe_2$) layers via a postgrowth tellurization reaction at 330 °C. The converted 2D $PdTe_2$ layers display a significant reduction in the bandgap energy from 0.7 to 0 eV accompanying thickness-invariant metallic characteristics, verified by a variety of spectroscopic techniques.

RESULTS

Figure 1a outlines a schematic for the CVD growth of thickness-controlled wafer-scale 2D $PdSe_2$ layers and the tellurization reaction for their conversion to 2D $PdTe_2$ layers. For the CVD growth, a thickness-controlled Pd film is deposited onto a silicon dioxide/silicon (SiO_2/Si) wafer by an electron beam deposition at a rate of about 0.05 Å/s. Subsequently, the Pd deposited-SiO_2/Si wafer is reacted with a vaporized Se at 330 °C for 60 min, following the temperature ramping rate of 10 °C/min. During the reaction, argon (Ar) gas is continuously supplied into the CVD chamber at a flow rate of ∼100 standard cubic centimeters per minute (SCCM) and at a pressure of 100 mTorr. For the conversion reaction, as-prepared 2D $PdSe_2$ layers are reacted with vaporized Te instead of Se under the exactly identical conditions employed for the CVD growth reaction at 330 °C. Figure 1b depicts the Raman spectroscopy analysis of 2D $PdSe_2$ layers prepared with five different Pd thickness of 2.1, 3.3, 5.8, 7.4, and 15.2 nm. Raman peaks corresponding to A_g and B_g vibration modes are distinctively observed at 143.6, 205.3, 220.8, and 255.7 cm^{-1}, which perfectly aligns with earlier studies on 2D $PdSe_2$ layers.[31] Furthermore, we inspected the location-specific spatial uniformity of single samples. Figure 1c presents Raman spectra of a representative sample of 2D $PdSe_2$ layers prepared with 2.1 nm Pd, collected from the randomly selected locations on a large area of >100 μm^2 (inset image). Nearly identical Raman characteristics are identified, which strongly supports the high spatial homogeneity of 2D $PdSe_2$ layers within/across samples. Figure 1d provides atomic force microscopy (AFM) profiles of the samples prepared with various Pd thickness, where the distance-dependent height variations denote the thickness of 2D $PdSe_2$ layers with respect to the surfaces of bare substrates. A representative AFM topography image along with a line scan orientation (red line) is also provided in the inset. Figure 1e shows a linear relation in the thickness of Pd films vs 2D $PdSe_2$ layers determined by AFM characterizations, indicating a thickness increase of ∼2.5 times through the CVD seleniztion. The inset presents an AFM topography image of 2D $PdSe_2$ layers prepared with 5.8 nm Pd in a projected view. Additional AFM images of samples prepared with various Pd thicknesses are presented in Supporting Information, Figure S1. As-

https://doi.org/10.1021/acsnano.4c11627
ACS Nano 2024, 18, 35336−35346

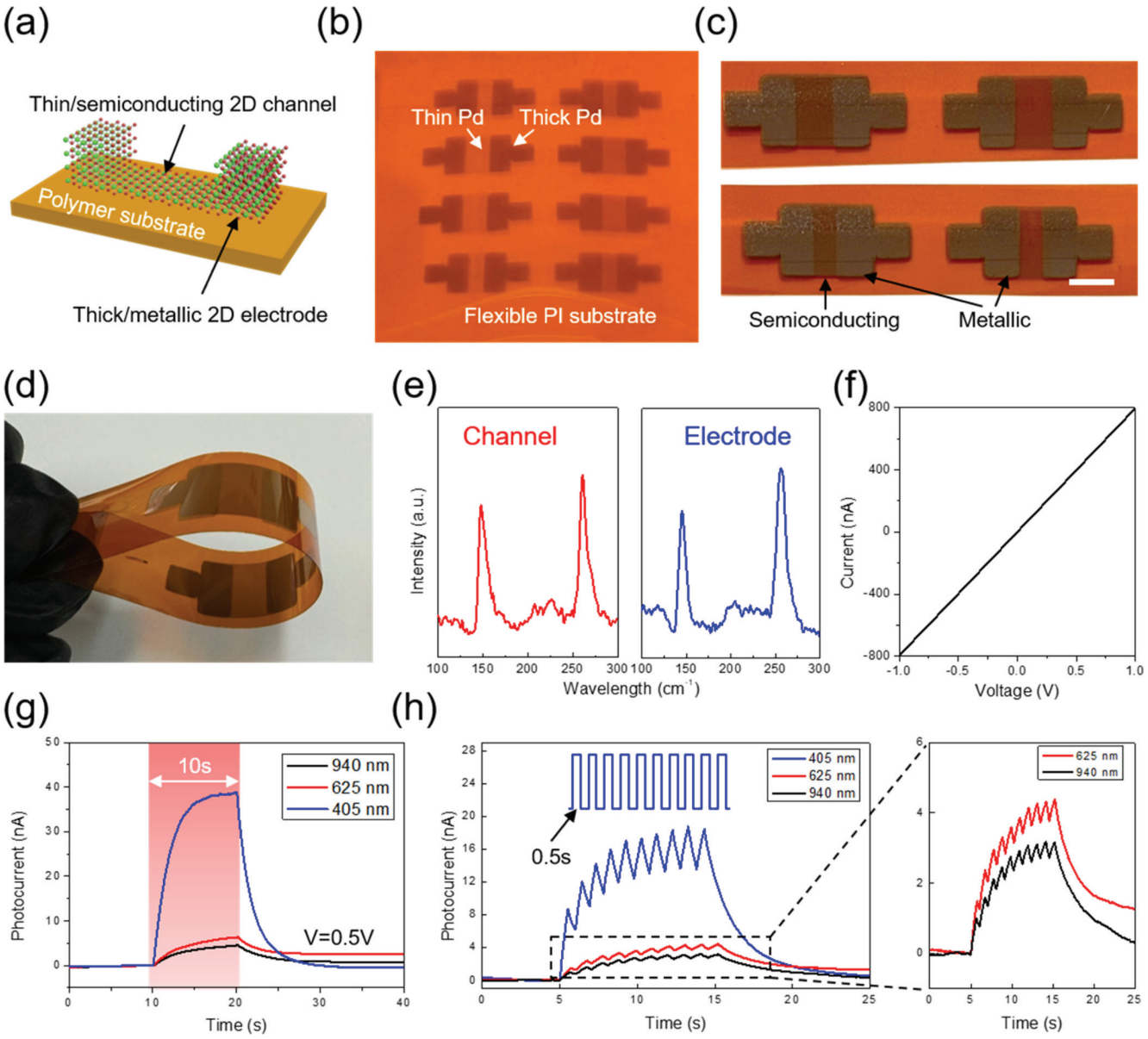

Figure 3. Application of thickness-variant semiconducting-to-metallic transition for all-2D $PdSe_2$ layers-based flexible devices. (a) Schematic of all-2D flexible device employing thickness-modulated 2D $PdSe_2$ layers. (b) Image of thickness-modulated Pd arrays patterned on PI substrate. (c) Image of patterned thin/thick 2D $PdSe_2$ layers. The scale bar is 5 mm. (d) Mechanical bending of patterned thin/thick 2D $PdSe_2$ layers on PI substrate. (e) Raman spectra obtained from thin channels and thick electrodes. (f) $I-V$ curve showing Ohmic transport. (g) Temporal plot of photoresponsiveness under continuous illuminations for 10 s at three different wavelengths. (h) Temporal plot of broadband synaptic plasticity under optical pulse illuminations with 0.5 s intervals. The smaller photocurrents for 625 and 940 nm wavelengths reflect their lower illumination intensities compared to that of 405 nm illumination.

prepared 2D $PdSe_2$ layers were characterized via transmission electron microscopy (TEM) imaging and diffraction techniques, toward better clarifying their thickness-microstructure correlation. Figure 1f depicts high-resolution TEM (HR-TEM) images of thickness-varying samples taken at an identical magnification, revealing lattice fringes regardless of thickness variations. Figure 1g displays selected area electronic diffraction (SAED) patterns corresponding to the thickness-variant 2D $PdSe_2$ layers in Figure 1f. The multiple diffraction rings observed in each sample are indexed to the crystalline planes of $PdSe_2$ crystals in an orthorhombic structure with a P_{bca} space group, characterized by lattice parameters of a = 5.75 Å, b = 5.87 Å, and c = 7.69 Å.[9,11,32]

Having verified the structural morphology of 2D $PdSe_2$ layers, we systematically investigated their thickness-dependent electrical properties by employing field effect transistor (FET) characterizations. Figure 2a inset provides a schematic illustration of a SiO_2/Si back-gate FET featuring thickness-variant 2D $PdSe_2$ layers as a channel. Figure 2a presents FET characteristics of drain-source current (I_{ds}) vs voltage (V_{ds}) with a varying back-gate voltage (V_g) obtained from a 2D $PdSe_2$ layers-incorporated FET (Pd thickness = 2.1 nm). The FET exhibits a strong p-type gate response manifested by a systematic decrease of I_{ds} with increasing V_g. Figure 2b presents the corresponding FET transfer curve of I_{ds} vs V_g obtained at V_{ds} = 1 V, further supporting the p-type

https://doi.org/10.1021/acsnano.4c11627
ACS Nano 2024, 18, 35336−35346

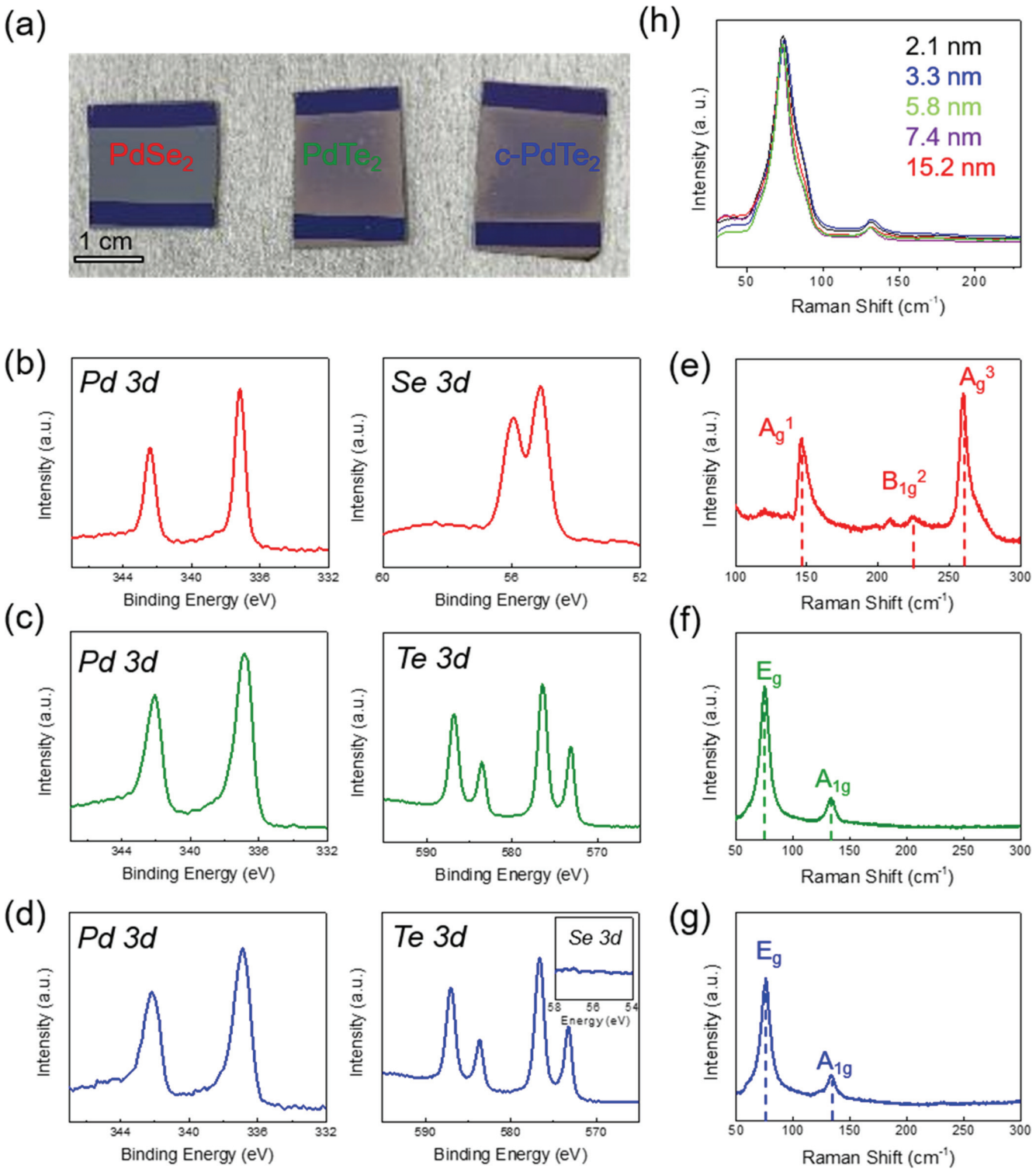

Figure 4. Anion exchange-driven conversion of 2D $PdSe_2$ layers to 2D $PdTe_2$ layers and its spectroscopic characterization. (a) Sample images of as-prepared $PdSe_2$ and $PdTe_2$ layers as well as converted (c) $PdTe_2$ layers. (b)−(d): XPS core binding energy spectra of; (b) as-prepared $PdSe_2$, (c) as-prepared $PdTe_2$, and (d) c-$PdTe_2$ layers. (e)−(g): Raman spectra of; (e) as-prepared $PdSe_2$, (f) as-prepared $PdTe_2$, and (g) c-$PdTe_2$ layers.

semiconducting transport. The linear regime (red tangential line) of the FET yields its hole mobility[30,33] which is determined to be ~2.32 $cm^2/V{\cdot}s$. Meanwhile, FETs incorporating thick 2D $PdSe_2$ layers exhibit completely distinct characteristics, as presented in Figure 2c,2d. For example, Figure 2c provides $I_{ds}-V_{ds}$ plots of a FET employing 2D $PdSe_2$ layers prepared with Pd thickness of 7.4 nm, revealing negligible gate responses with varying V_g. Figure 2d presents the corresponding FET transfer curve of I_{ds} vs V_g, which further confirms that the FET employing thick 2D $PdSe_2$ layers exhibits metallic characteristics without noticeable gate responses. For an accurate assessment of thickness-variant

https://doi.org/10.1021/acsnano.4c11627
ACS Nano 2024, 18, 35336−35346

FET characteristics, we fabricated various 2D $PdSe_2$ layers-based FETs by systematically modulating their thickness using identical fabrication conditions; i.e., direct sellenization of Pd films prepatterned by identical shadow masks. Figure 2e shows a plot of I_{ds} ratios measured at $V_g = \pm 60$ V for FETs employing 2D $PdSe_2$ layers of various thickness, prepared in identical fabrication batches. An abrupt increase of I_{ds} ratios is observed at Pd thickness of ~3 nm which corresponds to ~7.5 nm thick 2D $PdSe_2$ layers, while the ratios nearly saturate to unity beyond the thickness. In fact, thicker 2D $PdSe_2$ layers prepared with Pd thickness of slightly larger than 3 nm (e.g., 5.8 nm) exhibit much relaxed *p*-type semiconducting characteristics accompanying a reduced mobility of ~0.77 $cm^2/V{\cdot}s$, as presented in Supporting Information, Figure S2. This observation confirms a prominent and drastic onset of thickness-dependent semiconducting-to-metallic transitions in wafer-scale 2D $PdSe_2$ layers. In order to gain more insights about the semiconducting characteristics observed with small Pd thickness and their device preparation dependency, we also fabricated FETs employing semiconducting 2D $PdSe_2$ layers of various channel lengths. The fabrication was performed by e-beam lithography patterning techniques and a representative image of an array of fabricated FETs is presented in Figure 2f. The array contains a number of FETs with varying channel lengths; i.e., 3, 5, 7, and 10 μm, and the inset shows an image of a 10 μm-channel FET. Figure 2g shows $I_{ds}-V_g$ FET transfer curves with varying channel lengths along with their corresponding mobility values, revealing strong *p*-type gate responses. A maximum hole mobility of 2.36 $cm^2/V{\cdot}s$ is observed at a channel length of 3 μm, and this mobility value is similar to those of FETs fabricated by the direct patterned growth of 2D $PdSe_2$ layers with shadow masks (Figure 2b). Figure 2h presents V_g-dependent $I_{ds}-V_{ds}$ curves corresponding to the 3 μm channel FET, further confirming its strong semiconducting characteristics. Figure 2i presents a correlation of mobility value vs channel length, clarifying that FETs with shorter channels yield higher mobilities.

Application opportunities of the thickness-modulated semiconducting-to-metallic transition characteristics were explored by a scalable and monolithic fabrication of all-2D patterned arrays; i.e., flexible devices employing thin (thick) semiconducting (metallic) 2D $PdSe_2$ layer channels (electrodes) in a single platform. Figure 3a illustrates a schematic of the proposed all-2D flexible device composed of thin/thick $PdSe_2$ layer arrays, highlighting their atomically sharp interfaces. The device is fabricated on a polymeric polyamide (PI) substrate via a direct CVD growth of 2D $PdSe_2$ layers on it, enabled by the low reaction temperature of 330 °C. Figure 3b shows a representative image of thin/thick Pd patterned arrays sequentially prepared on a PI substrate by a stencil printing technique using a shadow mask. Details about the stencil printing process are described in Supporting Information, Figure S3. Figure 3c displays images of isolated patterned arrays of thin (2.1 nm Pd)/thick (7.4 nm Pd) $PdSe_2$ layers, obtained from a direct CVD tellurization of the sample in Figure 2h. Figure 3d demonstrates an excellent mechanical bendability of this all-2D $PdSe_2$ layers-based device. Figure 3e presents Raman spectra obtained from the same sample revealing nearly identical characteristics in both thin/semiconducting and thick/metallic regions. This observation confirms the monolithic and spatially localized growth of thickness-modulated 2D $PdSe_2$ layers even on flexible PI substrates. Figure 3f shows a current−voltage ($I-V$) plot of the same sample, revealing a formation of highly Ohmic contacts at the interfaces of thin/semiconducting layers and thick/metallic layers. Figure 3g showcases a photoresponsiveness of this flexible device under continuous 10 s illuminations at three different wavelengths of 405, 625, and 940 nm. The significant increase of photocurrents measured at a bias of 0.5 V confirms that the semiconducting 2D $PdSe_2$ layer channels efficiently generate electron−hole pairs which are collected by the metallic 2D $PdSe_2$ layer electrodes. Figure 3h presents a photoresponsiveness obtained from a periodically applied optical pulses with 0.5 s intervals. The photocurrents are observed to steadily increase during the illumination periods of total 10 s while they slowly decay once the illuminations are terminated. This observation indicates that the device exhibits characteristics of optically modulated synaptic plasticity which is strongly dependent on illumination frequencies, as observed in our previous studies[34,35] These synaptic characteristics are observed at a broad spectrum of visible-to-near-infrared (NIR), i.e., ranging from 405 to 625 and 940 nm (zoom-in view), indicating the device's intrinsic broadband responsiveness.

Beyond establishing the transition characteristics by the physical thickness modulation, we explored an anion exchange-based chemical method of introducing semiconducting-to-metallic transitions in 2D $PdSe_2$ layers. Thin semiconducting 2D $PdSe_2$ layers initially prepared with 2.1 nm Pd thickness were directly tellurized and completely converted to 2D $PdTe_2$ layers, as described in Figure 1a. Figure 4a shows photographs of three independently prepared samples of as-grown 2D $PdSe_2$ and $PdTe_2$ as well as converted-$PdTe_2$ (c-$PdTe_2$) layers. X-ray photoelectron spectroscopy (XPS) characterizations were performed on these samples with a major emphasis on identifying the chemical structure of c-$PdTe_2$ to unveil the Se-to-Te anion exchange efficacy. Figure 4b shows XPS core-level spectra of Pd 3d and Se 3d obtained from as-grown 2D $PdSe_2$ layers, revealing binding energy peaks consistent with earlier studies.[27] Figure 4c shows XPS core-level spectra of Pd 3d and Te 3d obtained from separately prepared 2D $PdTe_2$ layers whose peak characteristics are highly consistent with previous observations.[36] Figure 4d presents XPS core-level spectra of Pd 3d and Te 3d corresponding to the initial sample of $PdSe_2$ in Figure 4b after its subsequent conversion to c-$PdTe_2$. Interestingly, the XPS characteristics of c-$PdTe_2$ are exactly identical to those of as-grown $PdTe_2$ in Figure 4c, which indicates a Se-to-Te exchange-driven complete conversion of $PdSe_2$-to-$PdTe_2$. Specifically, the Se 3d peaks observed at the binding energy of 60-to-52 eV range in Figure 4b is observed to completely disappear, as clarified in the inset plot of Figure 4d right. Furthermore, Raman spectroscopy characterizations were performed to further confirm the anion exchange conversion of $PdSe_2$-to-$PdTe_2$. Figure 4e presents a Raman spectrum of the as-grown $PdSe_2$ sample corresponding to Figure 4b with well-resolved A_g and B_g characteristic peaks. Figure 4f presents a Raman spectrum of the as-grown $PdTe_2$ sample corresponding to Figure 4c, revealing peaks at 75 and 133 cm^{-1} associated with in-plane E_g and out-of-plane A_{1g} vibration modes of $PdTe_2$, respectively, consistent with previous observations.[37] Figure 4g displays a Raman spectrum of the c-$PdTe_2$ sample converted from $PdSe_2$, which exhibits exactly identical characteristics to those of Figure 4f. In fact, all the peaks observed with as-grown 2D $PdSe_2$ layers in Figure 4e are no longer present in Figure 4g, further supporting the complete conversion of $PdSe_2$-to-$PdTe_2$. Figure 4h presents Raman spectra obtained from multiple samples of c-$PdTe_2$

https://doi.org/10.1021/acsnano.4c11627
ACS Nano 2024, 18, 35336−35346

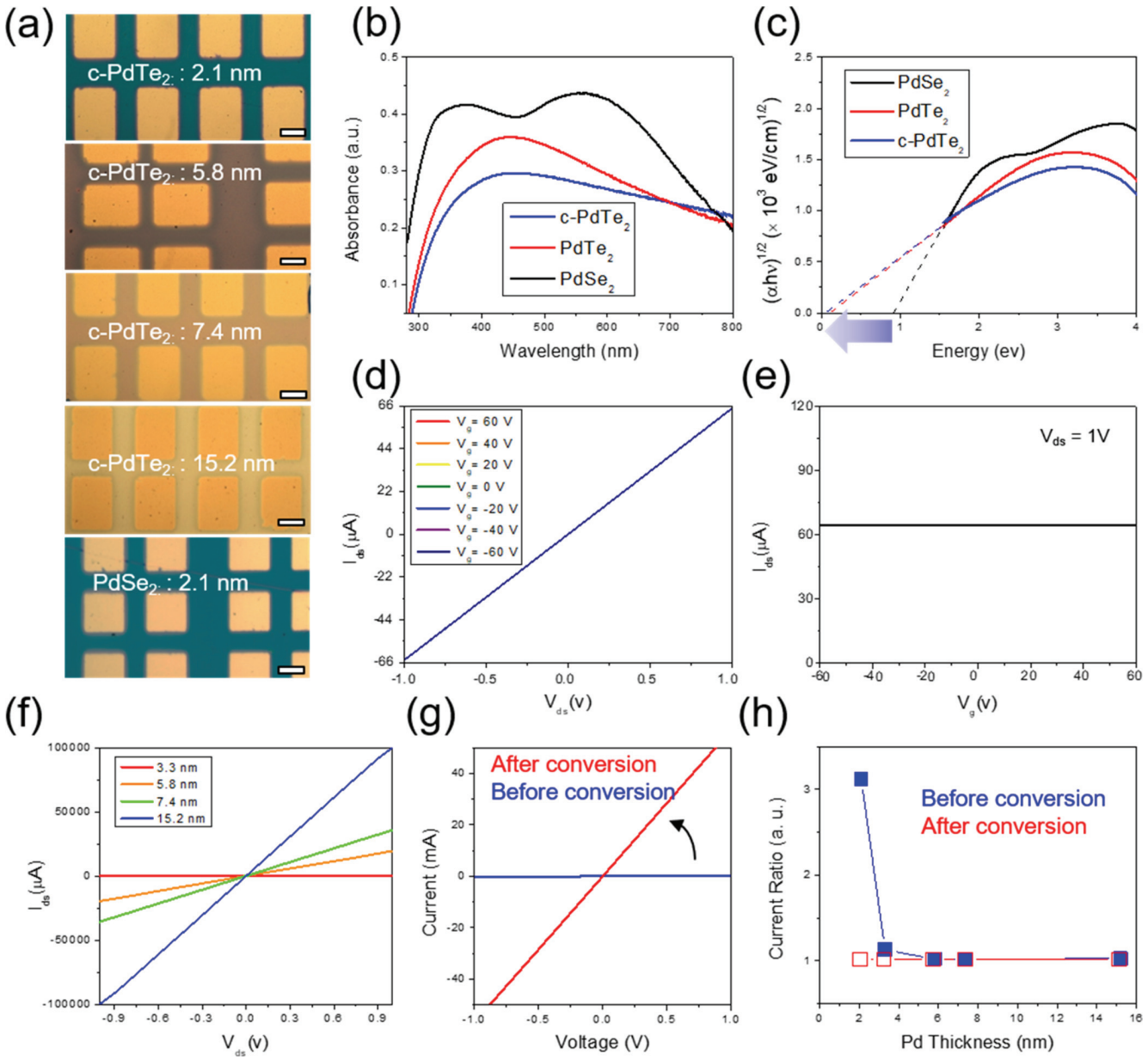

Figure 5. Semiconducting-to-metallic transition associated with conversion of 2D $PdSe_2$ layers to 2D $PdTe_2$ layers. (a) Optical microscopy images of Au electrodes-patterned c-$PdTe_2$ layers prepared with various Pd thickness as well as as-prepared $PdSe_2$ layers. The scale bars in all images are 100 μm. (b, c) Optical property comparison of as-prepared $PdSe_2$ and $PdTe_2$ as well as c-$PdTe_2$ layers characterized by (b) UV−vis absorbance, and (c) Tauc plots. (d) $I_{ds}-V_{ds}$ curves obtained from a FET employing c-$PdTe_2$ layers converted from thin $PdSe_2$ layers (Pd thickness = 2.1 nm). (e) $I_{ds}-V_g$ curve obtained from the same FET in (d) at V_{ds} = 1 V. (f) Comparison of $I_{ds}-V_{ds}$ curves obtained from c-$PdTe_2$ FETs with varying Pd thicknesses at V_g = 0 V. (g) Comparison of two-terminal $I-V$ characteristics for 2D $PdSe_2$ layers before/after their conversion. (h) Comparison of I_{ds} ratios at $V_g = \pm 60$ obtained from FETs employing as-prepared $PdSe_2$ (blue) vs c-$PdTe_2$ (red) layers as a function of Pd thickness.

prepared with various Pd thickness. The identical peak characteristics irrespective of Pd thickness variations support the highly homogeneous nature of the conversion process which involves minimal sample-to-sample variations. It is noteworthy that similar anion exchange-based conversions have been demonstrated in Pt-based 2D and 3D materials.[34,38]

Possible transitions of the electrical and/or optical properties of 2D $PdSe_2$ layers associated with their anion exchange-driven conversion were inspected by FET and spectroscopic measurements. Figure 5a shows a series of optical microscopy images of gold (Au) top electrodes-patterned c-$PdTe_2$ samples prepared with various Pd thickness fabricated for electrical measurements. Highly homogeneous color (thus, uniform morphology) and its progressive change are observed, which is also compared to the color of as-prepared 2D $PdSe_2$ layers before their conversion (bottom image). Energy band structures of samples before/after the conversion were inspected and compared by ultraviolet (UV)−visible spectroscopy. Figure 5b presents UV−visible absorbance spectra of samples in three different states of pristine 2D $PdSe_2$ and $PdTe_2$ as well as c-$PdTe_2$ layers. The optical absorbance of the $PdSe_2$ sample is observed to be higher than those of both

https://doi.org/10.1021/acsnano.4c11627
ACS Nano 2024, 18, 35336−35346

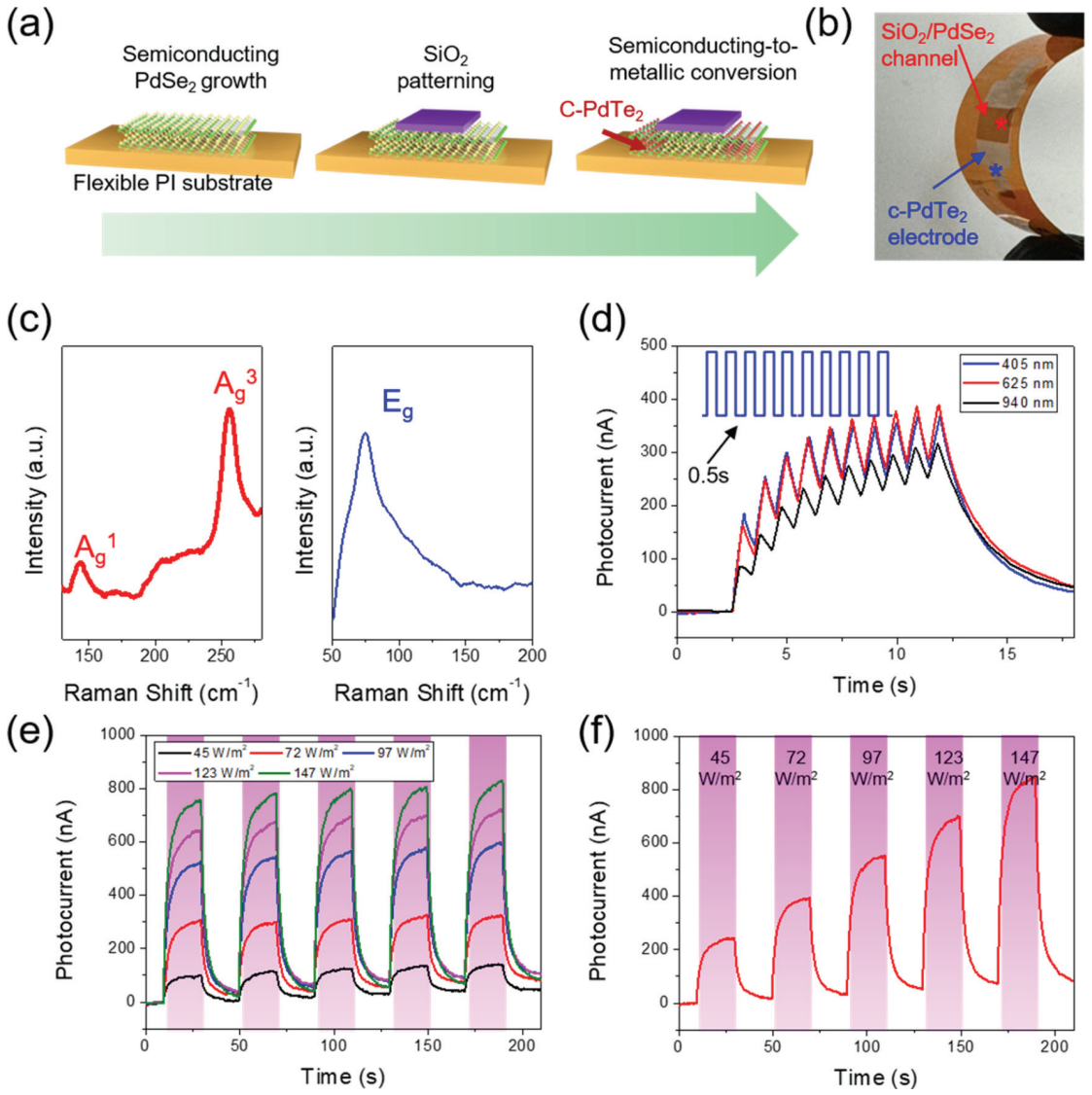

Figure 6. Application of anion exchange-driven semiconducting-to-metallic transition for all-2D $PdSe_2$ layers-based flexible devices. (a) Schematics to illustrate fabrication procedures for all-2D $PdSe_2$/c-$PdTe_2$ in-plane heterojunction device employing site-specific anion exchange reaction. (b) Image of all-2D flexible device composed of SiO_2/$PdSe_2$ channel interfaced with c-$PdTe_2$ electrodes. (c) Raman spectra obtained from the red and blue marks in Figure (b), revealing $PdSe_2$ (left) and $PdTe_2$ (right) characteristics, respectively. (d) Temporal plot of broadband synaptic plasticity under optical pulse illuminations with 0.5 s intervals. (e) Temporal plots of photoresponsiveness with long 20 s illumination intervals and varying intensities. (f) Illumination intensity-dependent photoresponsiveness.

$PdTe_2$ and c-$PdTe_2$ samples and is in good agreement with earlier studies on 2D $PdSe_2$ layers fabricated differently.[34] Furthermore, Tauc plots are extracted from the absorbance spectra, which yields bandgap energies of the three samples.[34] Figure 5c presents the corresponding Tauc plots of energy vs $(\alpha h\nu)^{0.5}$, where α represents the absorption coefficient, h is Planck's constant, and ν is the velocity of light. Bandgap energies are determined by extrapolating the linear tangents to the plots at the intercepts of the x-axis. An indirect bandgap value of ~0.7 eV is obtained for the $PdSe_2$ sample confirming its semiconducting nature, consistent with previous studies.[9,24,27] Meanwhile, both the $PdTe_2$ and c-$PdTe_2$ samples exhibit nearly negligible bandgap energies, indicating their metallic properties. Particularly, it is interesting to note that the c-$PdTe_2$ sample was converted from thin semiconducting 2D $PdSe_2$ layers, which indicates that the anion exchange conversion leads to notable semiconducting-to-metallic transitions. These chemically driven transition characteristics were also characterized by FET measurements. Figure 5d presents $I_{ds}-V_{ds}$ plots of a c-$PdTe_2$-based FET, which reveals metallic transports of V_g-independent negligible gate responses. The results are interesting given that the c-$PdTe_2$ FET channel was converted from thin semiconducting 2D $PdSe_2$ layers, highly consistent with optical characterizations in Figure 5c. Figure 5e shows the corresponding $I_{ds}-V_g$ FET transfer curve, which further supports the metallic nature of the c-$PdTe_2$ converted from semiconducting 2D $PdSe_2$ layers. Various FET $I_{ds}-V_g$ curves of c-$PdTe_2$-based FETs prepared with different Pd thickness are presented in Supporting Information, Figure S4. Figure 5f presents a comparison of $I_{ds}-V_{ds}$ curves for c-$PdTe_2$ FETs converted from 2D $PdSe_2$ layers prepared with various Pd thicknesses, measured at $V_g = 0$ V. A steady increase in I_{ds} is observed with increasing Pd thickness, while the conductance values of c-$PdTe_2$ FETs are much higher than those observed

https://doi.org/10.1021/acsnano.4c11627
ACS Nano 2024, 18, 35336−35346

before the conversion; for example, typically >100 times conductance increase before vs after conversion. In fact, Figure 5g compares two-terminal $I-V$ characteristics of an identical 2D $PdSe_2$ layers-based device before/after their conversion, revealing a conductance increase from 1.46×10^4 S/m (before; blue line) to 1.68×10^4 S/m (after; red line). Figure 5h compares plots of I_{ds} ratios measured at $V_g = \pm 60$ V for FETs employing 2D $PdSe_2$ layers of various thickness before/after their conversion. It is noted that the thickness-dependent onset of the semiconducting-to-metallic transitions in 2D $PdSe_2$ layers at ~3 nm Pd thickness no longer appears after their conversion to c-$PdTe_2$. Additionally, TEM-SAED analysis conducted on an identical sample of 2D $PdSe_2$ layers before/after the conversion confirms a preservation of their poly crystalline structures associated with the electrical transitions (Supporting Information, Figure S5). These comprehensive optical and electrical characterizations strongly support that 2D $PdSe_2$ layers undergo semiconducting-to-metallic transitions enabled by the Se-to-Te anion exchange. This chemistry-driven approach offers another degree of material property tunability in addition to the intrinsic physical thickness-modulated transitions, vastly broadening the applicability of wafer-scale 2D $PdSe_2$ layers in digital electronics and/or optoelectronics.

Similar to the demonstration of all-2D flexible devices by their thickness control in Figure 3, we also employed the anion exchange-driven conversion process to fabricate all-2D $PdSe_2$/c-$PdTe_2$ lateral heterojunction flexible devices; i.e., semiconducting $PdSe_2$ channels are seamlessly interfaced with metallic c-$PdTe_2$ electrodes. Figure 6a illustrates the fabrication process of all-2D $PdSe_2$/c-$PdTe_2$ flexible devices, which begins with growing semiconducting 2D $PdSe_2$ layers directly on flexible PI substrates. Subsequently, SiO_2 is selectively patterned and deposited on the pregrown $PdSe_2$, serving as a protective layer for the underlying semiconducting channel. A subsequent CVD tellurization reaction converts the 2D $PdSe_2$ layers exposed outside of the SiO_2 protection layer to metallic c-$PdTe_2$ layers. Figure 6b displays a photograph of an all-2D flexible device composed of a SiO_2/$PdSe_2$ channel laterally interfaced with c-$PdTe_2$ electrodes subjected to a mechanical bending. Figure 6c shows the Raman spectra corresponding to Figure 6b, with the spectra taken from the SiO_2/$PdSe_2$ channel region (left) and the c-$PdTe_2$ electrode regions (right). Distinct Raman peaks are observed in the channel vs electrode regions, consistent with spectral characteristics of 2D $PdSe_2$[31] and 2D $PdTe_2$[37] layers, respectively. This Raman analysis verifies that the deposited-SiO_2 layer efficiently protects its underlying 2D $PdSe_2$ layers against the subsequent tellurization reaction, while the exposed 2D $PdSe_2$ layers become fully converted to 2D $PdTe_2$ layers. This all-2D flexible device was employed to demonstrate optical synaptic characteristics as well as standard photodetection applications under modulated optical pulse conditions. Figure 6d presents a temporal plot of the photoresponsiveness obtained from the device illuminated at three different wavelengths of 405, 625, and 940 nm, by optical pulses with short 0.5 s intervals. Similar to the observations with all-2D thin/thick $PdSe_2$ layers in Figure 3h, the device exhibits wavelength-independent broadband characteristics of optically introduced synaptic plasticity (i.e., optical potentiation), essential for optoelectronic artificial synapse applications.[35] The device was further inspected with optical illuminations accompanying much longer pulse intervals. Figure 6e presents intensity-dependent photoresponsiveness characteristics of the same device under periodically applied 625 nm illuminations with 20 s intervals, measured at 1 V. A complete decay of the generated photocurrent is observed at each illumination cycle of 20 s, unlike the observations with much shorter intervals in Figure 6d. Figure 6f shows a temporal photoresponsiveness of the device with systematically increasing illumination intensities. These comprehensive optical measurement data confirm the semiconducting nature of 2D $PdSe_2$ layers capable of yielding electron–hole pairs under broadband illuminations, which are efficiently collected by seamlessly connected metallic 2D $PdTe_2$ layers. Additional data of intensity-dependent photoresponsiveness obtained under illuminations at three different wavelengths are also presented in Supporting Information, Figure S6. Lastly, FET characteristics of our wafer-scale CVD-grown 2D $PdSe_2$ layers are compared to those of previously reported CVD-2D $PdSe_2$ layers, and its corresponding comparison table is presented in Supporting Information, Figure S7.

CONCLUSIONS

In conclusion, we report on two independent approaches of physically or chemically introducing semiconducting-to-metallic transitions in wafer-scale 2D $PdSe_2$ layers grown at low temperatures. We envision that a judicious combination of these physical–chemical methods should be able to provide an excellent controllability of manipulating complex functionalities in the materials. Accordingly, this study is believed to be highly encouraging toward exploring all-2D devices adopting both metallic and semiconducting components in atomically thin forms.

METHODS

Growth of 2D $PdSe_2$ and $PdTe_2$ Layers, and Conversion of 2D $PdSe_2$-to-$PdTe_2$. Pristine 2D $PdSe_2$ and $PdTe_2$ layers were grown by CVD selenization and tellurization reactions, respectively. Initially, Pd films with various thicknesses were deposited onto SiO_2/Si (300 nm SiO_2 thickness) substrates by an electron beam evaporator (Thermionics E-beam Evaporator) at a fixed evaporation rate of 0.05 Å/s. The Pd-coated substrates were positioned in the central heating zone of a horizontal quartz tube CVD furnace (Lindberg/Blue M Mini-Mite). Alumina boats containing precursor powders (selenium: 99.9% and tellurium: 99%, Millipore Sigma) were placed upstream in the quartz tube. The system was evacuated to a base pressure of ~25 mTorr and was subsequently purged with Ar gas for 10 min to eliminate residual organics within in the tube. The furnace was then heated at a rate of 11 °C/min to 330 °C and was held at that temperature for 60 min for both selenization and tellurization reactions. During the reactions, the furnace was supplied with a continuous Ar gas flow of ~150 standard cubic centimeters per minute (sccm). For the $PdSe_2$-to-$PdTe_2$ conversion, as-grown 2D $PdSe_2$ layers were subjected to the CVD tellurization reaction under the identical conditions as described above.

Structural, Chemical, and Optical Characterizations. HR-TEM and SAED analyses were conducted using a FEI Tecnai F30 TEM. Raman spectroscopy was performed using a Horiba LaRAM HR Evolution Nano system with a 532 nm laser source. XPS characterization was carried out using an Escalab 250Xi system. UV–visible optical absorbance spectra were acquired in transmittance mode using a UV–vis spectrophotometer (Evolution 220). For the optical characterization, 2D $PdSe_2$, $PdTe_2$, and c-$PdTe_2$ layers were directly grown on optically transparent willow glass substrates.

FET Fabrication and Electrical Measurements. For the fabrication of back-gated FETs, Au contacts (50 nm) were deposited onto 2D $PdSe_2$, $PdTe_2$, and c-$PdTe_2$ layers using shadow masks to pattern the source and drain electrodes. For the inspection of the 2D $PdSe_2$ channel length-dependent FET performances, a direct laser

https://doi.org/10.1021/acsnano.4c11627
ACS Nano 2024, 18, 35336–35346

lithography was employed to define various micrometer-scale channel lengths using a 405 nm diode laser. All FET measurements were conducted at room temperature in ambient conditions using a home-built micromanipulator probe station paired with a semiconductor parameter analyzer (HP 4156A).

Fabrication of All-2D Flexible Devices and Photoresponsiveness Measurements. All-2D flexible devices with laterally interfaced semiconducting/metallic heterostructures were fabricated on PI substrates. The first strategy employed the thickness-variant semiconducting-to-metallic transition in all-2D $PdSe_2$ layers. In this approach, thin/thick Pd films were prepatterned and deposited in array forms using a thermionic electron beam evaporation and shadow masks. The patterned Pd/PI arrays were subsequently selenized under the previously described CVD conditions, yielding all-2D semiconducting/metallic $PdSe_2$ layers. The second strategy involved the anion exchange-driven semiconducting-to-metallic transition in 2D $PdSe_2$ layers. Thin semiconducting 2D $PdSe_2$ layers were directly grown on PI substrates using the same CVD conditions described above. Subsequently, SiO_2 (70 nm thickness) protection layers were deposited over the central region of the as-grown 2D $PdSe_2$ layers. Then, CVD tellurization reactions were employed, converting the 2D $PdSe_2$ layers exposed outside of the SiO_2 layers to metallic 2D $PdTe_2$ layers. The reactions were performed at 330 °C for 5 min under Ar flow of 150 sccm, accompanying a ramp rate of 13.2 °C/min. For both the thickness variation and anion exchange approaches, Au contacts were deposited onto the metallic 2D layers defining source and drains. Photoresponsiveness characterizations of the all-2D flexible heterostructure devices were carried out using LED lasers at wavelengths of 405, 625, and 940 nm as well as the home-built probe station.

ASSOCIATED CONTENT

Supporting Information

The Supporting Information is available free of charge at https://pubs.acs.org/doi/10.1021/acsnano.4c11627.

AFM images, FET transfer curves, Fabrication details, TEM/SAED images, Photoresponsiveness, and FET comparison table (PDF)

AUTHOR INFORMATION

Corresponding Author

Yeonwoong Jung − *Department of Materials Science and Engineering, University of Central Florida, Orlando, Florida 32816, United States; NanoScience Technology Center, University of Central Florida, Orlando, Florida 32826, United States; Department of Electrical and Computer Engineering, University of Central Florida, Orlando, Florida 32816, United States;* orcid.org/0000-0001-6042-5551; Email: yeonwoong.jung@ucf.edu

Authors

Alireza Ghanipour − *Department of Materials Science and Engineering, University of Central Florida, Orlando, Florida 32816, United States; NanoScience Technology Center, University of Central Florida, Orlando, Florida 32826, United States*

Sang Sub Han − *NanoScience Technology Center, University of Central Florida, Orlando, Florida 32826, United States*

Changhyeon Yoo − *NanoScience Technology Center, University of Central Florida, Orlando, Florida 32826, United States*

Chung Won Lee − *NanoScience Technology Center, University of Central Florida, Orlando, Florida 32826, United States*

Complete contact information is available at: https://pubs.acs.org/10.1021/acsnano.4c11627

Author Contributions

Y.J. conceived and directed the project. A.G. prepared all samples, conducted device measurements, and performed data analyses with assistance from S.S.H. and C.Y. S.S.H. performed TEM, XPS characterizations and photoresponsiveness measurements. C.Y. performed AFM measurements. C.W.L. performed Raman characterizations. A.G. and Y.J. wrote the manuscript incorporating data and inputs from all authors.

Notes

The authors declare no competing financial interest.

ACKNOWLEDGMENTS

Y.J. acknowledges financial support from the US National Science Foundation (CAREER: 2142310). S.S.H. acknowledges financial support from the Preeminent Postdoctoral Program (P3) at UCF.

REFERENCES

(1) Wang, Q. H.; Kalantar-Zadeh, K.; Kis, A.; Coleman, J. N.; Strano, M. S. Electronics and Optoelectronics of Two-Dimensional Transition Metal Dichalcogenides. *Nat. Nanotechnol.* **2012**, *7*, 699−712.

(2) Chhowalla, M.; Jena, D.; Zhang, H. Two-Dimensional Semiconductors for Transistors. *Nat. Rev. Mater.* **2016**, *1*, No. 16052.

(3) O'Brien, M.; McEvoy, N.; Hanlon, D.; Hallam, T.; Coleman, J. N.; Duesberg, G. S.; et al. Transition Metal Dichalcogenide Growth via Close Proximity Precursor Supply. *Sci. Rep.* **2014**, *4*, No. 7374.

(4) Lin, Z.; Carvalho, B. R.; Kahn, E.; Lv, R.; Rao, R.; Terrones, H.; Pimenta, M. A.; Terrones, M. Defect Engineering of Two-Dimensional Transition Metal Dichalcogenides. *2D Mater.* **2016**, *3*, No. 022002.

(5) Chia, X.; Adriano, A.; Lazar, P.; Sofer, Z.; Luxa, J.; Pumera, M. Layered Platinum Dichalcogenides (PtS_2, $PtSe_2$, and $PtTe_2$) Electrocatalysis: Monotonic Dependence on the Chalcogen Size. *Adv. Funct. Mater.* **2016**, *26*, 4306−4318.

(6) Chen, E.; Xu, W.; Chen, J.; Warner, J. H. 2D Layered Noble Metal Dichalcogenides (Pt, Pd, Se, S) for Electronics and Energy Applications. *Mater. Today Adv.* **2020**, *7*, No. 100076.

(7) Pandey, S. K.; Das, R.; Mahadevan, P. Layer-Dependent Electronic Structure Changes in Transition Metal Dichalcogenides: The Microscopic Origin. *ACS Omega* **2020**, *5*, 15169−15176.

(8) Priyanka; Kumar, R.; Chand, F. Tuning of Electronic and Optical Properties of PtS_2 Monolayer Using Stacking Engineering. *Phys. Status Solidi B* **2023**, *260*, No. 2300132.

(9) Oyedele, A. D.; Yang, S. Z.; Liang, L. B.; Puretzky, A. A.; Wang, K.; Zhang, J. J.; Yu, P.; Pudasaini, P. R.; Ghosh, A. W.; Liu, Z.; et al. $PdSe_2$: Pentagonal Two-Dimensional Layers with High Air Stability for Electronics. *J. Am. Chem. Soc.* **2017**, *139*, 14090−14097.

(10) Ansari, L.; Monaghan, S.; McEvoy, N.; Ó Coileáin, C.; Cullen, C. P.; Lin, J.; Siris, R.; Stimpel-Lindner, T.; Burke, K. F.; Mirabelli, G.; Duffy, R.; Caruso, E.; Nagle, R.; Duesberg, G. S.; Hurley, P.; Gity, F. Quantum Confinement-Induced Semimetal-to-Semiconductor Evolution in Large-Area Ultra-Thin $PtSe_2$ Films Grown at 400 °C. *npj 2D Mater. Appl.* **2019**, *3*, 33 DOI: 10.1038/s41699-019-0116-4.

(11) Sun, M.; Chou, J. P.; Shi, L.; et al. Few-Layer $PdSe_2$ Sheets: Promising Thermoelectric Materials Driven by High Valley Convergence. *ACS Omega* **2018**, *3*, 6502−6510.

(12) Long, M. S.; Wang, Y.; Wang, P.; Zhou, X. H.; Xia, H.; Luo, C.; Huang, S. Y.; Zhang, G. W.; Yan, H. G.; Fan, Z. Y.; et al. Palladium Diselenide Long-Wavelength Infrared Photodetector with High Sensitivity and Stability. *ACS Nano* **2019**, *13*, 2511−2519.

(13) Wang, Y.; Pang, J.; Cheng, Q.; Han, L.; Li, Y.; Meng, X.; Ibarlucea, B.; Zhao, H.; Yang, F.; Liu, H.; Liu, H.; Zhou, W.; Wang, X.; Rummeli, M. H.; Zhang, Y.; Cuniberti, G. Applications of 2D-

Layered Palladium Diselenide and Its van der Waals Heterostructures in Electronics and Optoelectronics. *Nano-Micro Lett.* **2021**, *13*, 143.
(14) Zhang, K.-C.; Cheng, L.-Y.; Shen, C.; Li, Y.-F.; Liu, Y.; Zhu, Y. Thickness-Dependent Anisotropic Transport of Phonons and Charges in Few-Layered $PdSe_2$. *Phys. Chem. Chem. Phys.* **2021**, *23*, 18869.
(15) Zhang, X.; Dai, M.; Deng, W.; Zhang, Y.; Wang, Q. J. A Broadband, Self-Powered, and Polarization-Sensitive $PdSe_2$ Photodetector Based on Asymmetric van der Waals Contacts. *Nanophotonics* **2023**, *12*, 607−618.
(16) Zeng, L. H.; Wu, D.; Lin, S. H.; Xie, C.; Yuan, H. Y.; Lu, W.; Lau, S. P.; Chai, Y.; Luo, L. B.; Li, Z. J.; Tsang, Y. H. Controlled Synthesis of 2D Palladium Diselenide for Sensitive Photodetector Applications. *Adv. Funct. Mater.* **2019**, *29*, No. 1806878.
(17) Liang, Q.; Wang, Q.; Zhang, Q.; Wei, J.; Lim, S. X.; Zhu, R.; Hu, J.; Wei, W.; Lee, C.; Sow, C. H.; Zhang, W.; Wee, A. T. S. High-Performance, Room Temperature, Ultra-Broadband Photodetectors Based on Air-Stable $PdSe_2$. *Adv. Mater.* **2019**, *31*, No. 1807609.
(18) Zhao, Y.; Song, J.-G.; Ryu, G. H.; Ko, K. Y.; Woo, W. J.; Kim, Y.; Kim, D.; Lim, J. H.; Lee, S.; Lee, Z.; Park, J.; Kim, H. Low-Temperature Synthesis of 2D MoS_2 on a Plastic Substrate for a Flexible Gas Sensor. *Nanoscale* **2018**, *10*, 9338−9345.
(19) Wang, Z.; Ali, N.; Ngo, T. D.; Shin, H.; Lee, S.; Yoo, W. J. Achieving Ultrahigh Electron Mobility in $PdSe_2$ Field-Effect Transistors via Semimetal Antimony as Contacts. *Adv. Funct. Mater.* **2023**, *33*, No. 2301651.
(20) Lei, W.; Zhang, S.; Heymann, G.; Tang, X.; Wen, J.; Zheng, X.; Hu, G.; Ming, X. A New 2D High-Pressure Phase of $PdSe_2$ with High-Mobility Transport Anisotropy for Photovoltaic Applications. *J. Mater. Chem. C* **2019**, *7*, 2096−2105.
(21) Ma, Y.; Kou, L.; Li, X.; et al. Room Temperature Quantum Spin Hall States in Two-Dimensional Crystals Composed of Pentagonal Rings and their Quantum Wells. *NPG Asia Mater.* **2016**, *8*, No. e264.
(22) Lin, J. H.; Zuluaga, S.; Yu, P.; Liu, Z.; Pantelides, S. T.; Suenaga, K. Novel Pd_2Se_3 Two-Dimensional Phase Driven by Interlayer Fusion in Layered $PdSe_2$. *Phys. Rev. Lett.* **2017**, *119*, No. 016101.
(23) Lu, L.-S.; Chen, G.-H.; Cheng, H.-Y.; Chuu, C.-P.; Lu, K.-C.; Chen, C.-H.; Lu, M.-Y.; Chuang, T.-H.; Wei, D.-H.; Chueh, W.-C.; Jian, W.-B.; Li, M.-Y.; Chang, Y.-M.; Li, L.-J.; Chang, W.-H. Layer-Dependent and In-Plane Anisotropic Properties of Low-Temperature Synthesized Few-Layer $PdSe_2$ Single Crystals. *ACS Nano* **2020**, *14* (4), 4963.
(24) Sun, J.; Shi, H.; Siegrist, T.; Singh, D. J. Electronic, Transport, and Optical Properties of Bulk and Monolayer $PdSe_2$. *Appl. Phys. Lett.* **2015**, *107*, No. 153902.
(25) Gu, Y.; Cai, H.; Dong, J.; Puretzky, A. A.; Briggs, D.; Rouleau, C. M.; Chisholm, M. F.; Unocic, R. R.; Mandrus, D.; Geohegan, D. B.; Xiao, K. Two-Dimensional Palladium Diselenide with Strong In-Plane Optical Anisotropy and High Mobility Grown by Chemical Vapor Deposition. *Adv. Mater.* **2020**, *31*, No. 1906238.
(26) Gu, Y.; Zhang, L.; Cai, H.; Liang, L.; Liu, C.; Hoffman, A.; Yu, Y.; Houston, A.; Puretzky, A. A.; Duscher, G.; Rack, P. D.; Rouleau, C. M.; Meng, X.; Yoon, M.; Geohegan, D. B.; Xiao, K. Stabilized Synthesis of 2D Verbeekite: Monoclinic $PdSe_2$ Crystals with High Mobility and In-Plane Optical and Electrical Anisotropy. *ACS Nano* **2022**, *16*, 13900−13910.
(27) Wei, M.; Lian, J.; Zhang, Y.; et al. Layer-Dependent Optical and Dielectric Properties of Centimeter-Scale $PdSe_2$ Films Grown by Chemical Vapor Deposition. *npj 2D Mater. Appl.* **2022**, *6*, 1−10.
(28) Zhao, X.; Zhao, Q.; Zhao, B.; Dai, X.-Q.; Wei, S.; Ma, Y. Electronic and Optical Properties of $PdSe_2$ from Monolayer to Trilayer. *Superlattices Microstruct.* **2020**, *142*, No. 106514.
(29) Oyedele, A. D.; Yang, S.; Feng, T.; Haglund, A. V.; Gu, Y.; Puretzky, A. A.; Briggs, D.; Rouleau, C. M.; Chisholm, M. F.; Unocic, R. R.; Mandrus, D.; Meyer, H. M., III; Pantelides, S. T.; Geohegan, D. B.; Xiao, K. Defect-Mediated Phase Transformation in Anisotropic 2D $PdSe_2$ Crystals for Seamless Electrical Contacts. *J. Am. Chem. Soc.* **2019**, *141*, 15644−15652.
(30) Zhang, R.; Zhang, Q.; Jia, X.; Wen, S.; Wu, H.; Gong; Yin, Y.; Lan, C.; Li, C. Thickness-Dependent Carrier Transport of $PdSe_2$ Films Grown by Plasma-Assisted Metal Selenization. *Nanotechnology* **2023**, *34* (34), No. 345704.
(31) Zhang, H.; Ma, P.; Zhu, M.; Zhang, W.; Wang, G.; Fu, S. Palladium Selenide as a Broadband Saturable Absorber for Ultra-Fast Photonics. *Nanophotonics* **2020**, *9*, 2557−2567, DOI: 10.1515/nanoph-2020-0116.
(32) Langer, J.; Jimenez de Aberasturi, D.; Aizpurua, J.; Alvarez-Puebla, R. A.; Auguié, B.; Baumberg, J. J.; Bazan, G. C.; Bell, S. E.; Boisen, A.; Brolo, A. G.; et al. Present and Future of Surface-Enhanced Raman Scattering. *ACS Nano* **2020**, *14* (1), 28−117.
(33) Han, S. S.; Kim, J. H.; Noh, C.; Kim, J. H.; Ji, E.; Kwon, J.; Yu, S. M.; Ko, T.-J.; Okogbue, E.; Oh, K. H.; Chung, H.-S.; Jung, Y.; Lee, G.-H.; Jung, Y. Horizontal-to-Vertical Transition of 2D Layer Orientation in Low-Temperature Chemical Vapor Deposition-Grown $PtSe_2$ and Its Influences on Electrical Properties and Device Applications. *ACS Appl. Mater. Interfaces* **2019**, *11*, 13598−13607.
(34) Han, S. S.; Shin, J. C.; Ghanipour, A.; Lee, J.-H.; Lee, S.-G.; Kim, J. H.; Chung, H.-S.; Lee, G.-H.; Jung, Y. High Mobility Transistors and Flexible Optical Synapses Enabled by Wafer-Scale Chemical Transformation of Pt-Based 2D Layers. *ACS Appl. Mater. Interfaces* **2024**, *16*, 36599−36608.
(35) Lee, C. W.; Yoo, C.; Han, S. S.; Song, Y.-J.; Kim, S. J.; Kim, J. H.; Jung, Y. Centimeter-Scale Tellurium Oxide Films for Artificial Optoelectronic Synapses with Broadband Responsiveness and Mechanical Flexibility. *ACS Nano* **2024**, *18* (28), 18635−18649, DOI: 10.1021/acsnano.4c04851.
(36) Zeng, L.; Han, W.; Ren, X.; Li, X.; Wu, D.; Liu, S.; Wang, H.; Lau, S. P.; Tsang, Y. H.; Shan, C.-X.; Jie, J. Uncooled Mid-Infrared Sensing Enabled by Chip-Integrated Low-Temperature-Grown 2D $PdTe_2$ Dirac Semimetal. *Nano Lett.* **2023**, *23*, 8241−8248, DOI: 10.1021/acs.nanolett.3c02396.
(37) Li, E.; Zhang, R.-Z.; Li, H.; Liu, C.; Li, G.; Wang, J.-O.; Qian, T.; Ding, H.; Zhang, Y.-Y.; Du, S.-X.; Lin, X.; Gao, H.-J. High Quality $PdTe_2$ Thin Films Grown by Molecular Beam Epitaxy. *Chin. Phys. B* **2018**, *27*, No. 086804.
(38) Han, S. S.; Shawkat, M. S.; Lee, Y. H.; Park, G.; Li, H.; Chung, H.-S.; Yoo, C.; Mofid, S. A.; Sattar, S.; Choudhary, N.; Choi, J.-Y.; Jung, Y.; Kim, J. H.; Jung, Y. Wafer-Scale Anion Exchange Conversion of Nonlayered PtS Films to van der Waals Two-Dimensional $PtTe_2$ Layers with Negative Photoresponsiveness. *Chem. Mater.* **2022**, *34*, 6996−7005.

https://doi.org/10.1021/acsnano.4c11627
ACS Nano 2024, 18, 35336−35346